

Using the SMG scheme to study the Rayleigh-Taylor instability growth in solids

Gabi Luttwak

Dynamic-123D consulting, Haifa 3475859, Israel



ARTICLE INFO

Article history:

Received 31 December 2019

Revised 27 March 2020

Accepted 28 May 2020

Available online 2 June 2020

Keywords:

Rayleigh-Taylor instability

Elastic-plastic flow

SMG scheme VIP limiter

Lagrange hydrodynamics

ALE

MMALE

ABSTRACT

Rayleigh-Taylor instability RTI occurs while a less dense fluid is accelerating a denser one Rayleigh (1883); Taylor (1950)[1,2]. Under gravity the material strength damps and prevents RTI formation in solids. However, at higher accelerations RTI will prevail. The Staggered Mesh Godunov (SMG) scheme for Lagrangian Luttwak and Falcovitz (2006)[3] and ALE Luttwak and Falcovitz (2005)[4] hydrodynamics is applied to study the effect of yield strength on the RTI growth. A test problem is set up which extends for solids a well-known test for RTI growth in fluids Loubere et al. (2010)[5]. The SMG scheme employs frame-invariant slope limiters. The convex hull based VIP limiter Luttwak and Falcovitz (2011); Luttwak and Falcovitz (2010)[6,7] is used for vectors and oriented Bounding Box based limiter Luttwak (2015)[8] for the stress tensor. This way, we prevent numerical effects of symmetry breaking to interfere, while following the RTI growth.

© 2020 Elsevier Ltd. All rights reserved.

1. Introduction

Rayleigh-Taylor instability occurs at the interface between two fluids, when the less dense fluid is accelerating the denser one. Small perturbations present at the interface start to grow exponentially and eventually can lead to a turbulent mixing of the fluids. Lord Rayleigh [1] was the first to analyze this instability growth when a heavier fluid lies over a lighter one under the influence of gravity. Later, sir G.I. Taylor [2], considered the more general case of instability growth when the lighter fluid pushes the denser one, and thus the gradients of density ρ and pressure p at the interface point in opposite directions $\nabla\rho \cdot \nabla p < 0$. The fluid motion can be caused not only by the earth gravity but can be driven by other causes such as magnetic fields, high intensity laser pulses, high velocity impact or the detonation of high explosives. The effects of RTI are important in such diverse fields as geophysics, meteorology, earth climate, astrophysics, ordnance and inertial confinement.

Material strength can stabilize and even prevent the RTI growth. Therefore, most solids do not exhibit RTI under gravity. Thus, RTI growth in elastic plastic materials at lower pressures can only be investigated by taking soft solids with very small yield strength. Dimonte [9] accelerated yogurt with a Linear Electric Motor (LEM) while Polavarapu et al. [10] used mayonnaise accelerated by a rotating wheel. However under high pressures and accelerations the

RTI is observed in solids [11–17]. From these experiments it is possible to estimate the yield strength of the materials at high pressure.

The yield strength Y does increase with strain - η , (strain hardening) and for some materials with the strain rate too - $\dot{\eta}$. The strength is known to decrease with temperature T until it vanishes at the melt temperature T_m . The yield strength, like the shear modulus- G is expected to increase with pressure- p . The widely used phenomenological model due to Johnson and Cook [18], does not include the pressure dependence of the yield strength. As the RTI in solids becomes important at high pressures, this effect should not be ignored. On the other hand, the semi-empirical model of Steinberg et al. [19] does include the effect of strain, pressure and temperature and the model's parameters are available for many common materials. However it does not include strain rate dependence. Strain rate dependence would break scale invariance. At least for 240mm/s steel rods Taylor impact on a rigid wall, experimental results seem to preserve scale invariance [20]. For many materials strain rate effects are known to be present. The models of Steinberg and Lund [21] and the PTW model [22] take into account strain rate dependence too. There are also other, dislocations theory based models, like the Zerilli-Armstrong model [23], the MTS [24] and the more recent multi-scale strength model [16]. They all predict that the material strength increases with strain rate. This effect seems to be especially important at very high strain rates due to phonon drag (Barton et al. [16]). In this region there maybe also an anomalous increase of yield strength with the temperature (see Kanel [25]).

E-mail address: gabi@123d.com

While the interface perturbations are small, a linear analysis can be performed. For fluids this was done already by Lord Rayleigh [1] and by sir G.I. Taylor [2]. The result of the linear analysis is an exponential growth of the perturbations. For elastic-plastic materials linear analysis was performed by Miles [26], Drucker [27], Robinson and Swegle [13], Dimonte et al. [9,12], Piriz et al. [28,29], Colvin [30], Sun [31], and Bai et al. [32].

As the perturbations grow, the linear analysis is no longer valid, and the growth slows down. For general initial conditions and as instabilities grow, numerical simulations are the best choice to study RTI. For fluids, because of the high deformations which eventually lead to turbulent mixing, such simulations have been carried out with multi-material Eulerian codes (e.g. Youngs [33], Dimonte et al. [34] and Glimm et al. [35]). For three dimensional configurations, these calculations use meshes with 3×10^7 to 3×10^9 zones, and thus require a massively parallel supercomputer to run these problems. However, even at these resolutions, the results can strongly depend on the numerical scheme used.

Fortunately, there is a simple test problem for RTI growth in fluids, (see Loubere et al. [5]), which became standard to compare the performance of different numerical schemes. And this 2D test case requires a mesh of only about 3400 zones and can be easily run on any personal computer. The Staggered Mesh Godunov-SMG scheme (see Luttwak et al. [3,4]) has been already applied [36] to RTI growth in fluids. With the development of the oriented Bounding Box based limiters for tensors [8], we want to apply it to investigate RTI growth and damping in solids. The SMG scheme is somewhat similar to the compatible schemes of Caramana et al. [37] and the pseudo-viscosity of Christensen [38], but with unique features. The Lagrangian phase of the SMG scheme can capture shocks with sharp monotonic profiles. The SMG scheme employs frame-invariant limiters. The VIP- Vector Image Polygon based limiter is used for the velocity vector [6,7], and an oriented Bounding Box limiter [8] is used for the stress tensor. These limiters act as shock detectors to prevent numerical dissipation outside the shock neighborhood. The scheme has a strong mesh stabilizing effect, preventing hourglass instability. Therefore, it can handle problems which would otherwise fail in classical Lagrange codes due to grid distortion. But maybe this mesh stabilizing mechanism could also damp the RTI growth? By passing to a multimaterial ALE (MMALE) mode, earlier in the calculation, mesh distortion can be prevented and results can be compared.

In solids, depending on the yield strength, RTI can be either completely damped out, or alternatively it can grow and lead to a turbulent mixing of the two materials. The numerical dissipation present in the scheme can nonphysically contribute to this damping. Mesh imprinting and scheme dependent symmetry breaking can produce artificial perturbations in the flow which will be amplified by the RTI growth. Therefore, it is important to use a scheme which could minimize numerical dissipation mesh imprinting and symmetry breaking. The SMG scheme with frame invariant limiters which can pass continuously from a Lagrangian to an ALE and MMALE calculation seems a good candidate for this. As the RTI growth starts from small perturbations, the first numerical simulations to study RTI in solids were carried out in Lagrangian codes (e.g. Barnes [11], Swegle and Robinson [14]) or later with ALE codes [39]. Experiments to study RTI growth in solids must accelerate the plate isentropically, e.g. Barnes used a plane wave generator to initiate a high explosive. A gap between the charge to the plate formed a ramp wave in the plate (see Fig. 1 for a schematic view of such experiments). Numerical simulations to reproduce this have to mesh all the system. To study RTI growth in solids we propose a simpler test case. This extends the previously mentioned test case for fluids. It cannot replace simulations required to reproduce experiment but can help us to investigate the effect of yield strength and of the details of the numerical scheme on the

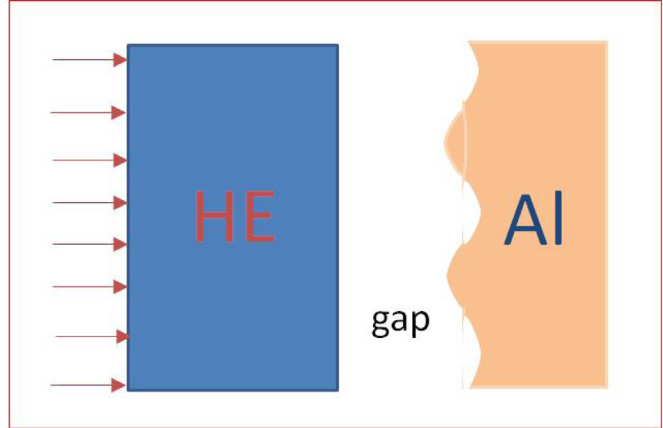


Fig. 1. A schematic view of RT experiment.

RTI growth. We also propose to use it to quickly compare different codes.

2. Theory

2.1. The staggered mesh godunov - SMG scheme

The SMG scheme described here is implemented in a three dimensional code. Two dimensional problems were solved by taking a single row of zones with the appropriate boundary conditions. The control volumes in Fig. 2 are depicted in 2D, but the same logic applies to 3D and unstructured meshes. Finite differences can be obtained by applying the conservation laws of mass momentum and energy over a moving control volume:

$$\frac{d}{dt} \int_V \rho dV = \int_{\partial V} \rho (\vec{v} - \vec{v}_g) \cdot d\vec{a} \quad (1)$$

$$\frac{d}{dt} \int_V \rho \vec{v} dV = \int_{\partial V} \rho \vec{v} (\vec{v} - \vec{v}_g) \cdot d\vec{a} + \int_{\partial V} \underline{\underline{\sigma}} \cdot d\vec{a} + \int_V \rho \vec{f}_b dV \quad (2)$$

$$\frac{d}{dt} \int_V \rho e_T dV = \int_{\partial V} \rho e_T (\vec{v} - \vec{v}_g) \cdot d\vec{a} + \int_{\partial V} \underline{\underline{\sigma}} \cdot \vec{v} \cdot d\vec{a} \quad (3)$$

Here ρ is the density, \vec{v} and \vec{v}_g are respectively the material and grid velocities, e and $e_T = e + 1/2(\vec{v} \cdot \vec{v})$ are the specific internal and total energies. \vec{f}_b represent body forces per unit mass. Thus, $\vec{f}_b = (0, -g, 0)$ for gravity. The stress tensor is split into the scalar pressure p and the deviatoric stress $\underline{\underline{\sigma}}$:

$$\underline{\underline{\sigma}} = -p \underline{\underline{1}} + \underline{\underline{\sigma}} \quad (4)$$

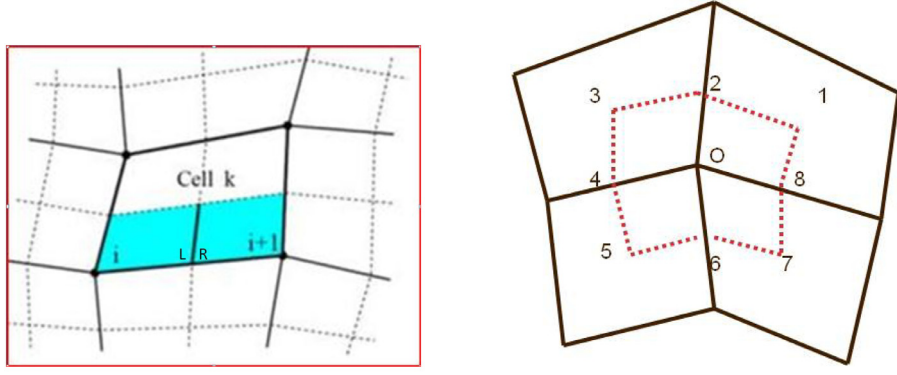
The material model closes the above equations. It includes an Equation of State-EOS $p = p(\rho, e)$, and a constitutive relation for the elastic plastic flow. This follows the classical Wilkins [40] approach. See also Maire et al. [41]. In an elastic region the deviatoric stress is advanced by an incremental Hooke law, corrected to take into account the stress rotation so as to make the Hooke law frame-independent:

$$\frac{d}{dt} \underline{\underline{s}}^{el} = 2G\dot{\underline{\underline{\epsilon}}} + \underline{\underline{\Omega}} \underline{\underline{s}} - \underline{\underline{s}} \underline{\underline{\Omega}} \quad (5)$$

Here $\underline{\underline{s}}$ is the current and $\underline{\underline{s}}^{el}$ is the predicted elastic deviatoric stress. Defining the frame-invariant Jaumann derivative $\frac{d}{dt} \underline{\underline{s}}^{el}$ we get:

$$\frac{d}{dt} \underline{\underline{s}}^{el} = \frac{d}{dt} \underline{\underline{s}}^{el} + \underline{\underline{s}} \underline{\underline{\Omega}} - \underline{\underline{\Omega}} \underline{\underline{s}} \quad (6)$$

$$\frac{d}{dt} \underline{\underline{s}}^{el} = 2G\dot{\underline{\underline{\epsilon}}} \quad (7)$$



(a) The zone and the corner zones

(b) The momentum control volume

Fig. 2. The staggered mesh godunov-SMG scheme.

Here, G is the shear modulus, $\underline{\dot{\eta}}$ is the deviatoric stain rate and $\underline{\Omega}$ is the spin tensor. For small changes of strain in one time step, these are obtained from the velocity gradient tensor $\nabla \vec{v}$ as:

$$\underline{\dot{\eta}} = 0.5(\underline{\nabla \vec{v}} + \underline{\nabla \vec{v}}^T) - \frac{1}{3}\nabla \cdot \vec{v} \underline{\mathbb{1}} \quad (8)$$

$$\underline{\Omega} = 0.5(\underline{\nabla \vec{v}} - \underline{\nabla \vec{v}}^T) \quad (9)$$

If \underline{s}_{eq}^{el} exceeds the yield criterion it is returned to the yield surface by radial return:

$$\underline{\underline{\sigma}} = \begin{cases} \frac{\underline{\gamma}}{s_{eq}^{el}} \underline{\underline{s}}^{el} & \text{if } s_{eq}^{el} \geq Y \\ \underline{\underline{s}}^{el} & \text{otherwise} \end{cases} \quad (10)$$

Here the equivalent stress is:

$$s_{eq} = \sqrt{3J_2} = \sqrt{3/2}|\underline{\underline{s}}|; \quad |\underline{\underline{s}}| = \sqrt{\underline{\underline{\sigma}} : \underline{\underline{\sigma}}} \quad (11)$$

with J_2 being the second invariant of the deviatoric stress. The change in the equivalent plastic strain in a time step is:

$$\Delta \eta_{eq}^{pl} = \begin{cases} \frac{s_{eq}^{el} - Y}{3G} & \text{for } s_{eq} > Y \\ 0 & \text{otherwise} \end{cases} \quad (12)$$

To get the total equivalent plastic strain, Eq. (12) is time integrated:

$$\eta_{eq}^{pl} = \int_0^T \Delta \eta_{eq}^{pl} dt \quad (13)$$

The equivalent plastic strain rate is obtained by dividing $\Delta \eta_{eq}^{pl}$ by the time step Δt :

$$\dot{\eta}_{eq}^{pl} = \frac{\Delta \eta_{eq}^{pl}}{\Delta t} \quad (14)$$

The zone centered velocity gradient $\underline{\nabla \vec{v}}$ is calculated by applying he Gauss theorem over the computational zone:

$$\underline{\nabla \vec{v}} = \frac{1}{V} \int_{\partial V} \vec{v} d\vec{a} = \frac{1}{V} \sum_f \vec{v}_f \vec{s}_f \quad (15)$$

The sum is over the faces f of the zone. \vec{s}_f is the face area vector and \vec{v}_f is the face f velocity taken as the average of the face node velocities. The time step is split into a Lagrangian phase followed by an advection phase. According to the grid motion prescription, the calculation can remain Lagrangian, single material ALE or full multimaterial MMALE. For a MMALE calculation, the material interfaces cut through the mesh lines. The advection phase must handle the interface reconstruction and the flux calculations.

2.1.1. The lagrangian phase

The Lagrangian phase is formulated using internal energy but by using a ‘compatible scheme’ [37] total energy can be conserved too. SMG is a staggered scheme. Therefore, the velocities are defined at nodes, while the densities ρ , internal energy e , and the stress tensor are zone centered. Unlike some other staggered schemes, the gradient of velocity $\nabla \vec{v}$ is also zone centered. Thus, there is a jump in velocity \vec{v} at the in-zone corner zone faces (see Fig. 2(a)) and a “simplified” Impact Riemann Problems (IRP) is solved there. The velocity jump is evaluated at mid-edge, between points L,R in Fig. 2(a)). This IRP is solved in the normal to the shock direction, assumed to lie along $\Delta \vec{v} = \vec{v}_{i+1} - \vec{v}_i$. The zone-centered velocity gradient $\nabla \vec{v}$ is limited to maintain a monotonic velocity profile using the frame-invariant Convex Hull based VIP limiter (see [6,7] and Section 2.1.2 here) for vectors. The limited velocity gradient $[\nabla \vec{v}]_{lim}$ is used to get left \vec{v}_L and right \vec{v}_R face velocities at the in-zone corner zone faces (see Fig. 2(a)):

$$\vec{v}_f = \vec{v}_n + [\nabla \vec{v}]_{lim} \cdot \Delta \vec{r}_{fn} \quad (16)$$

In Eq. (16), $f = L, R$ are taken respectively for $n = i, i+1$. The resulting velocity jump $\Delta \vec{v}_{LR} = \vec{v}_R - \vec{v}_L$ together with the zone centered variables make up the input data for the Impact Riemann problem. The pressure p^* resulting from the solution of the IRP acts on the corner zone faces. The deviatoric stress $\underline{\underline{\sigma}}$ defined at the zone center will also act on these faces. Integrating these contributions from all corner zone faces surrounding the vertex O (see Fig. 2(b)) would directly give its time-advanced velocity. Setting $p^* = p_k + (p^* - p_k)$, we prefer to split this process into two stages:

- First the contribution of zone stress $\sigma_k = \underline{\underline{\sigma}} - p_k \mathbb{1}$ is integrated around vertex O. Let $\vec{s}_{i,i+1}$ be the face vector of the in zone face separating corner zones i and $i+1$ in Fig. 2(a), pointing from node i to $i+1$. A force $\vec{F}_{i,i+1} = \sigma_k \cdot \vec{s}_{i,i+1}$ will act on the corner zone i and $-\vec{F}_{i,i+1}$ will act on $i+1$.
- The additional term $Q = p^* - p_k$ is treated as a uni-axial pseudo-viscosity, exerting a force only along the normal to shock direction taken along the edge neighbors velocity difference $\Delta \vec{v}_{i,i+1}$. That is, if $\hat{n} = \Delta \vec{v}_{i,i+1} / |\Delta \vec{v}_{i,i+1}|$, then:

$$\vec{F}_{i,i+1}^Q = -Q(\vec{s}_{i,i+1} \cdot \hat{n})\hat{n} \quad (17)$$

Again, $\vec{F}_{i,i+1}^Q$ acts on i and $-\vec{F}_{i,i+1}^Q$ on $i+1$. Thus, the total momentum is conserved. The velocity jump $\Delta \vec{v}_{LR}$ depends on the zone centered limited velocity gradient $[\nabla \vec{v}]_{lim}$ and it can be different in each of the zones around the edge $(i, i+1)$.

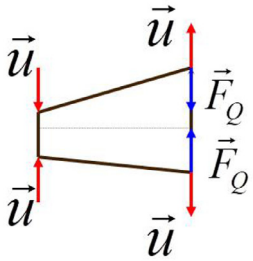


Fig. 3. SMG's mesh stabilizing effect.

The work done by all these forces is used to update the zone internal energy like in “compatible hydrodynamics” [37]:

$$\Delta e_k = -\frac{\sum_i \vec{F}_i \cdot \vec{v}_i}{m_k} \Delta t \quad (18)$$

In Eq. (18), Δe_k is the change in the internal energy in zone k , Δt is the time step, while the sum is over the N_k corner zones of zone k . m_k is the mass of zone k , \vec{v}_i is the velocity of node i and \vec{F}_i is a force acting on the corner zone i . The Q-forces thus generated by the SMG scheme tend to “naturally” attenuate hourglass instabilities as described in Luttwak and Falcovitz [42]. At a hourglass instability, the zone centered velocity gradient vanishes, and the whole node to node velocity difference contributes to the IRP solution along $\Delta \vec{v}_{i,i+1}$, acting as seen in Fig. 3. Unlike Caramana’s edge pseudo-viscosity, this Q-term acts both in expansion and in compression. This feature helps to fight the hourglass instability, but it is also necessary to simulate shocks which may occur in expansion, like reactive shocks during detonation initiation (see Luttwak et al. [43]) and rarefaction shocks.¹

2.1.2. The VIP-the vector image polygon/polyhedron

The VIP is [6,7,42] an extension of a 1D range to a vector-space (or tensor-space). Vectors and tensors are in-between their neighbors if they lie inside their convex hull (CH) (see Fig. 4). The convex hull spanned by points \vec{v}_i ; $i = 1 \dots n$ in the vector (or tensor) space can be defined as:

$$\vec{v} = \sum_{i=1}^n \alpha_i \vec{v}_i; \quad 0 \leq \alpha_i \leq 1; \quad \alpha_1 + \alpha_2 + \dots + \alpha_n = 1 \quad (19)$$

Which for $n=2$, it is thus a 1D range:

$$\vec{v} = \alpha \vec{v}_1 + (1 - \alpha) \vec{v}_2; \quad 0 \leq \alpha \leq 1 \quad (20)$$

which is similar for scalar v , v_1 , v_2 to a range defined by:

$$\min(v_1, v_2) \leq v \leq \max(v_1, v_2) \quad (21)$$

But while extending Eq. (21) for each vector component separately is not invariant under rotation, the VIP/TIP Vector or Tensor Image Polygon/Polyhedron based limiters are frame invariant. The gradients are limited by monotonic extrapolation [42]. For velocity this is done separately along each edge in a zone. The zone centered velocity gradient is limited, so that the outward extrapolated velocities from the edge two endpoints along the edge lie inside the convex hull generated by the neighboring nodes (see also [6]). This limited gradient is used to find the velocity jump at the edge mid-face which is required for the IRP solution.

¹ rarefaction shock waves can occur near a phase change in solids or when the isentrope is concave, i.e. $[\partial^2 p / \partial^2 v]_s < 0$, with p , v , s being respectively the pressure, the specific volume and the entropy.

2.1.3. The advection phase

For zone centered variables we compute the fluxes through the zone faces. The volume flux at the face into the zone is defined as the volume swept by that face when its nodes are moving, respectively, with the local fluid velocity \vec{v} and mesh velocity \vec{v}_g . Let $\vec{r}_{f,i}^{n+1,l} = \vec{r}_{f,i}^l + \vec{v}_{f,i}^l \Delta t$ and $\vec{r}_{f,i}^{n+1,g} = \vec{r}_{f,i}^g + \vec{v}_{f,i}^g \Delta t$, be the positions of the face nodes $i = 1, N_{f,n}$, advanced respectively with the material and grid velocities until $t + \Delta t$:

$$\Delta V_f = \text{Volume}(\{\vec{r}_{f,i}^{n+1,l}\}_{i=1}^{N_f}; \{\vec{r}_{f,i}^{n+1,g}\}_{i=1}^{N_f}) \quad (22)$$

With this definition, total volume is exactly conserved:

$$V^{n+1} = V^l + \Sigma_f \Delta V_f \quad (23)$$

Here V^l being the volume in the zone after the Lagrange step.

The densities at the fluxed volume center are evaluated by:

$$\rho_f = \rho_c + [\vec{\nabla} \rho]_{lim} \cdot \Delta \vec{r}_{fc} \quad (24)$$

from the density at the upstream zone center ρ_c , using $[\vec{\nabla} \rho]_{lim}$ - the limited ZC gradient. The ZC gradient is limited by scalar limiting [42], i.e. by multiplying it with the largest coefficient $0 \leq \alpha \leq 1$ such that the extrapolated densities at the zone nodes remain in the range defined by the density in the zone and its neighbors. Here $\Delta \vec{r}_{fc} = \vec{r}_f - \vec{r}_c$. \vec{r}_f is the center of this polyhedron and \vec{r}_c is the center of the upstream zone c . The mass flux at the face is $\Delta m_f = \rho_f \delta V_f$ and the mass in the zone is conserved:

$$m^{n+1} = m^l + \Sigma_f \Delta m_f; \quad \rho^{n+1} = \frac{m^{n+1}}{V^{n+1}} \quad (25)$$

$m^l = m^n$ is the mass after the Lagrange step which is the same as the mass m^n at $T = T^n$.

In a similar way the total energy flux (see Eq. (3)) is $\Delta E_T = \rho_f e_{T,f} \Delta V_f$ and the total energy is conserved:

$$E_T^{n+1} = m^l e_T^l + \Sigma_f \Delta E_{T,f}; \quad e_T^{n+1} = \frac{E_T^{n+1}}{m^{n+1}} \quad (26)$$

For convenience we flux separately the internal energy and let $\Delta E_f^i = \rho_f e_f^i \Delta V$ be the internal energy flux. Then we get:

$$E_i^{n+1} = m^l e_i^l + \Sigma_f \Delta E_{i,f}; \quad e_i^{n+1} = \frac{E_i^{n+1}}{m^{n+1}} \quad (27)$$

Using Eq. (26) we conserve total energy. The specific internal energy is obtained by removing the zone kinetic energy. Alternatively by using Eq. (27), e_i^{n+1} can be directly obtained, but in this case, total energy is not exactly conserved. In the present simulations we conserves total energy. Near a shock, total energy conservation maybe preferable. In problems where most of the energy is kinetic, small fluctuations in the kinetic energy can produce large fluctuations in the internal energy and through the equation of state also in the pressure. As stability requires the solution to be dissipative, a decrease in the kinetic energy may occur which can cause un-physical heating. For example this may cause melting near the axis, in the numerical simulation of a penetrating high speed jet. By fluxing separately internal and total energies it is possible to make the appropriate choice for a problem, or even in a specific region.

The deviatoric stress $\underline{\underline{s}}$ at the center of the fluxed volume is:

$$\underline{\underline{s}}_f = \underline{\underline{s}}_c + [\nabla \underline{\underline{s}}]_{lim} \cdot \Delta \vec{r}_{fc} \quad (28)$$

The deviatoric stress $\underline{\underline{s}}$ is advected as a volume weighted average:

$$\underline{\underline{s}}^{n+1} = \frac{V^l \underline{\underline{s}}^l + \Sigma_f \underline{\underline{s}}_f \Delta V_f}{V^{n+1}} \quad (29)$$

The plastic yield criterion is applied again to the updated values of $\underline{\underline{s}}$. Let:

$$[\nabla \underline{\underline{s}}]_{lim} = \alpha \nabla \underline{\underline{s}}; \quad 0 \leq \alpha \leq 1 \quad (30)$$

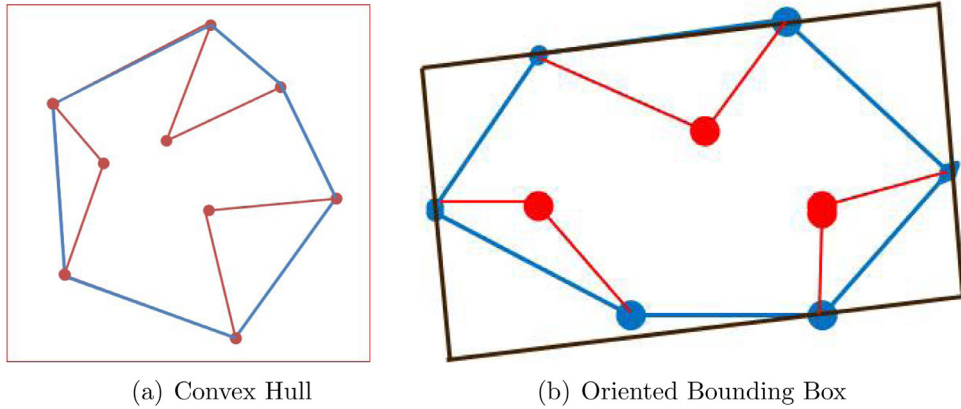


Fig. 4. Convex hull and oriented bounding box of points in 2D.

Here $0 \leq \alpha \leq 1$ is a constant to be determined. Let us denote:

$$\Delta \underline{s}_{fc} = \nabla \underline{s} \cdot \Delta \vec{r}_{fc} \quad (31)$$

Then Eq. (28) becomes:

$$\underline{s}_f = \underline{s}_c + \alpha \Delta \underline{s}_{fc} \quad (32)$$

α should be chosen so that s_f for the zone c all faces f will remain inside the neighborhood defined by s_c and the values s_m in the zones across the faces s_f . Using mesh-related or Cartesian components of s would be frame-dependent. Our frame-invariant limiter for the deviatoric stress is based on an oriented Bounding Box (BB) of the convex hull aligned along the CH diameter (see Luttwak [8] and following Section 2.1.4). The deviatoric stress is a symmetric trace-less tensor with five independent components. Let us define a five component vector $\vec{s} = (s_1, s_2, s_3, s_4, s_5)$:

$$\vec{s} = \left(\frac{s_{xx}\sqrt{3}}{2}, \frac{s_{yy} - s_{xx}}{2}, s_{xy}, s_{yz}, s_{xz} \right) \quad (33)$$

With this choice, $\vec{s}^2 = \vec{s} \cdot \vec{s}$ gives us the second invariant J_2 :

$$\vec{s} \cdot \vec{s} = J_2 = \frac{1}{2} Tr(s_{\perp}^2) \quad (34)$$

Using Eq. (33) we pass the deviatoric stresses $\underline{\underline{s}}_c$, $\underline{\underline{s}}_f$, $\Delta\underline{\underline{s}}_{fc}$ and $(\underline{\underline{s}}_n, n = 1, N_f)$ to the five-vectors \vec{s}_c , \vec{s}_f , $\Delta\vec{s}_{fc}$ and $(\vec{s}_n, n = 1, N_f)$. Here $f = 1, N_f$ are the N_f faces of zone c and $n = 1, N_f$ are the zones across these faces. As described in Section 2.1.4 we build the oriented BB around the vectors $\vec{s}_n, n = 1, N_f$. This BB defines 5 orthogonal directions in the vector space $(\hat{n}_j, j = 1, 5)$. We limit α so that \vec{s}_f remains inside the BB. This is done component-wise but the components are defined in the vector space. These directions are not mesh related and they are frame-invariant. Thus let $s_{f,j} = \vec{s}_f \cdot \hat{n}_j$ and $\Delta s_{fc,j} = \Delta\vec{s}_{fc} \cdot \hat{n}_j$ be the components along \hat{n}_j . Also, let $(s_j^{\min}, s_j^{\max}, j = 1, 5)$ be the min and max values of the BB in direction \hat{n}_j . Then:

$$\alpha_j = \begin{cases} \frac{s_j^{\min} - s_{f,j}}{|\Delta s_{fc,j}|} & \text{if } s_{f,j} < s_j^{\min} \\ \frac{s_j^{\max} - s_{f,j}}{|\Delta s_{fc,j}|} & \text{if } s_{f,j} > s_j^{\max} \\ 1 & \text{if } s_j^{\min} \leq s_{f,j} \leq s_j^{\max} \end{cases}; \quad \alpha = \min_{j=1}^5 \alpha_j \quad (35)$$

Face based fluxes do not directly take into account the “diagonal flow” between node neighbor zones that do not share a common face. This second order error is reduced with the partially split volume integration scheme [44]. That is, only changes due to the partial fluxes that would not perturb a steady flow are immediately updated. The remaining flux-divergence terms are saved and added

to all zones at the end of the ALE advection. In the SMG scheme, slope limiting for zone centered scalar variables is required solely during the ALE advection phase.

The momentum advection is carried out on the staggered mesh. Therefore momentum fluxes should be computed at the (in-zone) corner zone faces (see Fig. 2) which define the staggered mesh. To maintain consistency with the zone-centered fluxes, these are not explicitly computed. First, the volume and mass fluxes at the zone faces are split into the corresponding corner zone faces. These are the “external”, (not the in-zone) corner zone faces (like O2, O6 in Fig. 2(b)). The volume flux is computed as in Eq. (22), but for the corner zone faces. These are defined by their nodes (shown here for the face moving with \vec{v}^g) as:

- The node i : $\bar{r}_1^g = \bar{r}_{f,i}^{n+1,g}$
 - The center of edge $i : i + 1$: $\bar{r}_2^g = \bar{r}_{f,i:i+1}^{n+1,g} = (1/2)(\bar{r}_{f,i}^{n+1,g} + \bar{r}_{f,i+1}^{n+1,g})$
 - The corner zone face center: $\bar{r}_3^g = \bar{r}_{f,c}^{n+1,g} = (1/N_{fn}) \sum_f \bar{r}_{f,i}^{n+1,g}$
 - The center of edge $i - 1 : i$: $\bar{r}_4^g = \bar{r}_{f,i-1:i}^{n+1,g} = (1/2)(\bar{r}_{f,i-1}^{n+1,g} + \bar{r}_{f,i}^{n+1,g})$

$i - 1$ and $i + 1$ denote here the edge neighbors of node i on face f . Let $\Delta V_{f,i}$ be the flux volume, which is the volume enclosed between $\{\vec{r}_j^l\}_{j=1}^4$ and $\{\vec{r}_j^g\}_{j=1}^4$. The density is obtained again from the upstream zone from Eq. (24). The mass and momentum flux out of the corner zone i will be:

$$\Delta m_{f,i} = \rho_f \Delta V_{f,i}; \quad \Delta \vec{M}_{f,i} = \Delta m_{f,i} \vec{v}_f \quad (36)$$

\bar{v}_f is the material velocity of the fluxed volume. A reasonable approximation is to take it as the material velocity of node i :

$$\vec{v}_f = \vec{v}_{f,i}^{n+1,l} \quad (37)$$

We can improve this by taking the velocity at the fluxed volume center:

$$\vec{v}_f = \vec{v}_{f,i}^{n+1,l} + [\nabla \vec{v}]_{lim} \cdot \frac{1}{2} (\vec{r}_{f,i:i+1}^{n+1,l} - \vec{r}_{f,i:i+1}^{n+1,g}) \quad (38)$$

$[\nabla \vec{v}]_{lim}$ is taken from the upstream zone. The VIP limiter for vectors is used to get this limited ZC velocity gradient. Like in the Lagrange phase we assume that the corner zone i velocity is centered at the node i and not at the corner zone center.

At this stage we have computed the mass and momentum fluxes from the neighboring zones and into the corner zones of zone k . They are redistributed between the corner zones in the zone by Falcovitz's flow model (see Luttwak et al. [45]). During the Lagrange phase both the corner zone masses and the zone mass

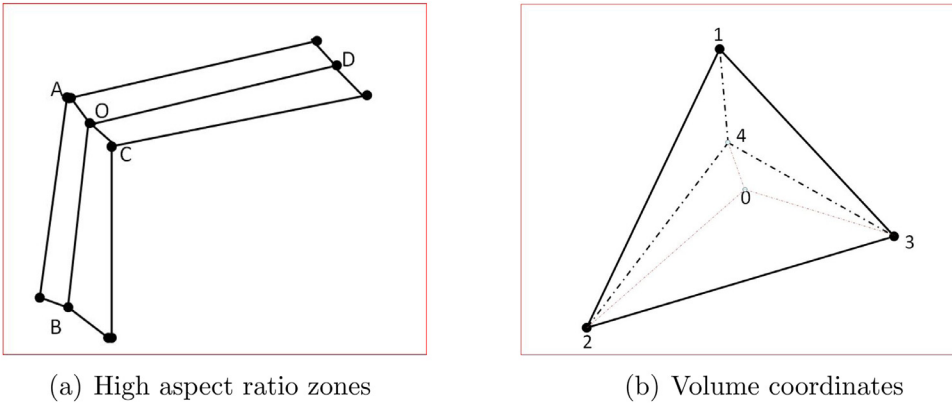


Fig. 5. The grid motion.

remain constant. Thus, their ratio $\Lambda_i = \frac{m_i}{\bar{m}}$ is also constant. Specifically for Wilkins scheme [40] it is $\Lambda_i = \frac{1}{N_k}$ or $\Lambda_i = \frac{1}{8}$ for a hexahedron. The final mass of corner zone i should be $\Lambda_i m$. Knowing the current mass m_i for each corner zone and assuming that there are mass fluxes only between face neighbor corner zones and that there is no circulation of mass, there is a unique solution for all these mass fluxes. (e.g. $\delta m_{i,i+1}$ in Fig. 2(a) and see [45]). If \vec{M}_i is the current momentum in the corner zone i , then $\delta \vec{M}_{i,i+1} = \frac{\delta m_{i,i+1}}{m_i} \vec{M}_i$ is the momentum flux from corner zone i to $i + 1$.

In the MMALE phase (see [47]), material boundaries cut through the mesh and a volume of fluid (VOF) interface reconstruction is used. It is based on the idea that the volume of the fluid and the normal to the interface uniquely determine its position [46,47]. See Luttwak [48] for more details.

2.1.4. The oriented bounding box (BB)

The symmetric stress tensor has six components and even the trace-less deviatoric stress will have five independent components. Thus, while the VIP limiter is well defined for tensors, building the convex hull in a 5 or 6 dimensional tensor space could be a challenging task. Instead, we define an Oriented Bounding Box (BB) (see [8]) as an approximation for the convex hull. We find the box direction by aligning it with the CH diameter. This is a physical direction in the sense of Maire [49]. Thus the Oriented Bounding Box limiter will be frame-invariant. Let us note that taking a box along Cartesian coordinates or other mesh related directions would be frame-dependent. Fortunately we are able to find the CH diameter without having to explicitly find the CH itself. Let $d_{ij} = |\vec{v}_i - \vec{v}_j|$ be the distance (in the vector or tensor space) between two points $i, j \in S$. The diameter, D is defined as:

$$D = \max_{i,j} d_{ij}; \quad \forall i, j \in S \quad (39)$$

Let i_1, i_2 be the first two points in S , such that $d(i_1, i_2) = D$, than we take the BB first normal, \hat{n}_1 , along the diameter:

$$\hat{n}_1 = \frac{\vec{v}_i - \vec{v}_j}{|\vec{v}_i - \vec{v}_j|} \quad (40)$$

Like the CH, the BB is defined in vector or tensor space and therefore it is frame invariant. After \hat{n}_1 was found, we look for the remaining orthogonal directions. The process is similar to the Gram-Schmidt construction to find an orthonormal base. We remove all components along \hat{n}_1 :

$$\vec{v}_i^t = \vec{v}_i - (\vec{v}_i \cdot \hat{n}_1) \hat{n}_1 \quad (41)$$

And proceed in a similar way to find the next normal along the diameter of the set spanned by $\{\vec{v}_i^t\}$.

2.1.5. The grid motion

A Lagrangian mesh moves and deforms with the material. Thus it cannot handle large deformations. An Eulerian mesh is fixed in space and can handle them easily, but it has to deal with large material fluxes flowing through the mesh. The purpose of the ALE grid motion is to reduce mesh distortion, while maintaining a smooth, near Lagrangian mesh. The grid motion algorithm used here was described in Luttwak and Rabie [47] and more in detail in Luttwak [50]. Each node moves toward a weighted average of its edge neighbors.

$$\vec{r}_o = \frac{\sum_{i=1}^n \omega_i \vec{r}_i}{\sum_{i=1}^n \omega_i} \quad (42)$$

Taking equal weights $\omega_i = 1; \forall i$ would generate an orthogonal mesh in a cubic region but could produce inverted zones for a mesh with a high aspect ratio. As shown in Fig. 5(a), using equal weights, point O could move outside its neighbor zones. This can be prevented by choosing larger weight for closer neighbors. Let us take weights:

$$\omega_i = \omega_j = \frac{1}{(\vec{r}_i - \vec{r}_j)^2} \quad (43)$$

Here \vec{r}_i, \vec{r}_j being any pair of edge neighbors along same mesh direction (e.g. points A,C, or points B,D in the Fig. 5). This requires a locally structured mesh. Using Eqs. (42) and (43) and iterating over the mesh several times in one time-step (typically $n_{iter} = 6$), we can preserve a smooth, almost orthogonal mesh. To keep the mesh motion almost Lagrangian we limit the grid motion per time step $\Delta \vec{r}.g = (\vec{v}^g - \vec{v}^l)\Delta t$ to be small relative to local mesh sizes, so that (in Eq. (23)):

$$\Delta V_f/V^l \leq k \quad \text{with e.g. } k \approx 0.2 \quad (44)$$

The results using Eqs. (42) and (43) are similar to those obtained using Winslow's scheme [51]. More general meshing algorithms like Knupp et al. [52] could be also applied here. Boundary points are allowed to slide on the boundary toward the weighted average (again using Eqs. (42) and (43)) of their in-boundary edge neighbors. The initial mesh of the test case was generated by bilinear interpolation. For larger perturbations they could first undergo smoothing iterations using Eqs. (42) and (43) before the beginning of the calculation.

To prevent the grid motion to change the local resolution of the initial mesh which could also cause un-necessary dissipation, we store volume coordinates (see [50]). Each mesh point \vec{r} is assumed to lie inside the polyhedron formed by its edge neighbors. Applying once Eqs. (42) and (43) we get a new point \vec{r}_n . This point splits the polyhedron into tetrahedra. Point \vec{r} will be located inside of one of them. The position of any point 0 (see Fig. 5(b)) inside a

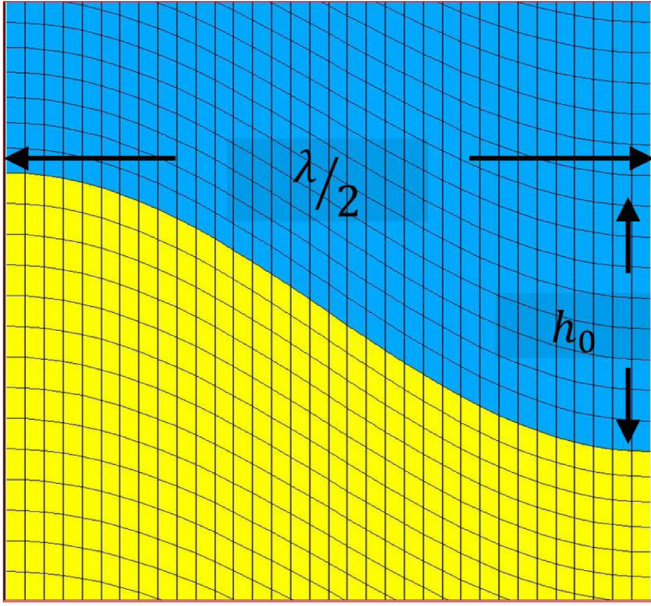


Fig. 6. The initial perturbation.

tetrahedron 1234 can be expressed as:

$$\vec{r}_0 = \sum_{i=1}^4 \alpha_i \vec{r}_i \quad \text{with} \quad \alpha_i = \frac{V_i}{V_{1234}}; \quad 0 \leq \alpha_i \leq 1; \quad \sum_{i=1}^4 \alpha_i = 1 \quad (45)$$

Here V_{1234} is the tetrahedron volume and V_i is the volume of the tetrahedron formed by point 0 and the face opposite to node i . At the start of the calculation we store three volume coordinates α_i ; $i = 1, 3$ at each mesh point and applying Eq. (45) we get back the position of \vec{r} . As the neighbor points move, we first apply Eqs. (42) and (43) to get \vec{r}_n and then use Eq. (45) to advance the mesh point \vec{r} .

2.2. The Rayleigh-Taylor instability (RTI)

While the amplitude h_0 (see Fig. 6) of the initial perturbations is small relative to the wave length λ , (i.e. $h_0 < \lambda$) a linear analysis can be carried out. In fluids the result is an exponential growth of the Rayleigh-Taylor Instability:

$$h(t) = h_0 e^{\gamma t}; \quad \gamma = \sqrt{A_T g k}; \quad A_T = \frac{\rho_2 - \rho_1}{\rho_2 + \rho_1}$$

A_T is the Atwood number, ρ_1, ρ_2 are the densities, $k = 2\pi/\lambda$ is the wave number, g is the gravity. $h(t)$ is the amplitude at time t . The hydrostatic pressure difference, from the perturbation base to its head, along h_0 is: $\Delta p_h = \Delta \rho g h_0$. Here $\Delta \rho = \rho_2 - \rho_1$. For an elastic plastic material, plastic flow will occur provided: $\Delta p_h > Y$, where Y is the yield strength:

$$Y < \Delta p_h = \Delta \rho g h_0 \quad (46)$$

Elastic flow will damp short waves if: $k > \frac{\rho g}{2G}$ (see Dimonte [9]), i.e. if:

$$\lambda < \frac{4\pi G}{\rho g} \quad (47)$$

As the amplitude $h(t)$ increases, the linear analysis is no longer valid, and the amplitude growth slows down. As bubbles grow and merge, for fluid their penetration depth grow like:

$$h(t) = \alpha A_T g t^2 \quad (48)$$

2.2.1. RTI test case for fluid flow schemes (from Loubere et al. [5])

A 2D space $[0 \leq x \leq \frac{1}{6}; 0 \leq y \leq 1]$ is filled with $\gamma = 1.4$ ideal gas. The initial density is:

$$\rho(x, y) = \begin{cases} \rho_1 = 1 & \text{if } y \leq y_i(x) \\ \rho_2 = 2 & \text{if } y > y_i(x) \end{cases} \text{ with } y_i(x) = 0.5 + 0.01 \cos(6\pi x) \quad (49)$$

Thus, the Atwood number, the wave amplitude and the wave length are:

$$A_t = \frac{1}{3}; \quad h_0 = 0.02; \quad \lambda_0 = \frac{1}{3} \quad (50)$$

The initial hydrostatic pressure distribution is:

$$p(x, y) = \begin{cases} p_0 + \rho_2 g (1 - y_i(x)) + \rho_1 g (y_i(x) - y) & \text{if } y \leq y_i(x) \\ p_0 + \rho_2 g (1 - y) & \text{if } y > y_i(x) \end{cases} \quad (51)$$

The gravity is: $g = a_y = -0.1$. Here $p_0 = 1$ is some initial added pressure. The initial specific energy is taken as :

$$e(x, y) = \frac{p(x, y)}{(\gamma - 1)\rho(x, y)} \quad (52)$$

The 2D box outside boundaries are reflecting sliding wall. We used a mesh with 34x100 zones and the problem is run until $T_{mx} = 10$.

2.2.2. RTI test case for solids

In the fluid test case the fluids are ideal gas and the units scale. For the solid test case we use SI units with mass, length and time (MLT): mg, mm, μs. Then the pressure p is in GPa and densities are in $\frac{\text{mg}}{\text{mm}^3}$. We replace the $\rho_2 = 2$ gas by an Aluminum (Al) layer of same width (0.5 mm) and $\rho_2 = 2.785 \frac{\text{mg}}{\text{mm}^3}$ thus $A_T = 0.47$. The gas density here is $\rho_1 = 1 \frac{\text{mg}}{\text{mm}^3}$. Instead of Eq. (49) we have:

$$\rho = \begin{cases} \rho_1 = 1 & \text{if } y \leq y_i(x) \\ \rho_2 = 2.785 & \text{if } y > y_i(x) \end{cases} \text{ with } y_i(x) = 0.5 + 0.01 \cos(6\pi x) \quad (53)$$

Again we assume an initial hydrostatic pressure distribution $p(x, y)$ which is obtained from Eq. (51), with $\rho_2 = 2.785$. The hydrostatic pressure at the Al-gas interface will be:

$$p_I = p_0 + 0.5 \rho_2 g = 0.1 + 1.3925 g \quad (54)$$

And as from the above, $h_0 = 0.02$, and $\Delta \rho = 1.785$, we get from Eq. (55) :

$$\Delta p_h = 0.0357 g \quad (55)$$

For Al we use a Mie-Gruneisen shock Equation of State (EOS):

$$p(\rho, e) = p_h + \Gamma \rho (e - e_h) \quad \text{with} \quad \eta = 1 - \rho_0/\rho \quad (56)$$

$$U_s = c_0 + s u_p; \quad p_h = \frac{\rho_0 c_0^2 \eta}{(1 - s \eta)^2} \quad (57)$$

$$e_h = \frac{1}{2} \frac{p_h}{\rho_0} \eta \quad (58)$$

Here U_s is the shock speed while c_0, u_p are the particle velocity and sound speed. ρ, e are the density and internal energy. p_h, e_h are the pressure and internal energy on the Hugoniot. For Al we take $c_0 = 5.328 \frac{\text{mm}}{\mu\text{s}}$, $\Gamma = 2$, $s = 1.338$. For a Mie-Gruneisen EOS with constant Γ we took instead of Eq. (52):

$$e(x, y) = \frac{p_y}{\Gamma \rho(x, y)} \quad (59)$$

The Steinberg et al. [19] model is used to get the yield strength and the shear modulus:

$$G(p, T) = G_0 \left[1 + \frac{G'_p}{G_0} \frac{p}{\delta^{1/3}} + \frac{G'_T}{G_0} (T - 300) \right]; \quad \delta = \rho/\rho_0 \quad (60)$$

$$Y(\eta, p, T) = \min(Y_0(1 + (\beta(\eta + \eta_i)^n), Y_{mx}) \\ \times \left[1 + \frac{Y'_p}{Y_0} \frac{p}{\delta^{1/3}} + \frac{G'_T}{G_0}(T - 300) \right] \quad (61)$$

Here $G(p, T)$, $Y(\eta, p, T)$ are respectively the yield strength and the shear modulus as a function of the pressure p , temperature T and strain η , while $G_0, Y_0, Y_{mx}, Y'_p, G'_T, \beta, n, \eta_i$ are the model parameters. Under earth gravity, $g = 10 \frac{\text{m}}{\text{s}^2} = 10^{-8} \frac{\text{mm}}{\mu\text{s}^2}$ and RTI growth would be damped out by material strength! However taking respectively $g = 0.1, 10, 100 \frac{\text{mm}}{\mu\text{s}^2}$, RTI growth can be investigated for different accelerations in this simple and reproducible test problem. This test case could be altered to use other Equation of State and Constitutive Relations. We could replace both layers in the fluid test case with different solids. Having only one solid layer has the advantage to make the problem depend on a single Yield strength parameter. For convenience, we left the $\rho = 1$ ideal gas layer, unchanged like in the fluid test. This means a $\rho = 1 \frac{\text{mg}}{\text{mm}^3}$ gas. The density of air is only about $0.0012 \frac{\text{mg}}{\text{mm}^3}$. To make a test case which could be also compared to experiments it would make sense to chose water for the $\rho = 1 \frac{\text{mg}}{\text{mm}^3}$ layer instead of ideal gas. In Section 3.5 we compare the results of ideal gas and water in one calculation.

3. Test calculations

We consider elastic-plastic flow with a constant shear modulus- G and yield strength- Y . For Al6061 we take [19] :

$$G_0 = 27.6 \text{ GPa}, Y_0 = 0.3 \text{ GPa}$$

By varying the Y , its effect on the RTI growth can be understood. Steinberg et al. model (see Eqs. (60) and (61)) and its parameters [19] are used to compute the yield strength $Y(\eta, p, T)$ and shear modulus $G(p, T)$ of the aluminum. In the following examples only the pressure and strain dependence of Y and pressure dependence of G was considered. We compare Lagrangian and MMALE SMG calculations with different constant values of the yield strength Y and the shear modulus G . We also consider and compare these

with the case when the yield strength $Y(p, \eta)$ and the shear modulus $G(p)$ are increasing functions of the pressure p . If the initial growth is exponential, to get similar deformation, for the accelerations g we will have to run the problem until:

$$T_{mx} \approx 1/\gamma \approx \frac{1}{\sqrt{g}} \quad (62)$$

First we consider elastic-plastic flow with a constant shear modulus- G and yield strength- Y . For Al6061 we take $G_0 = 27.6 \text{ GPa}$, $Y_0 = 0.3 \text{ GPa}$. By varying the Y , its effect on the RTI growth can be understood. $Y(p, \eta, T)$ and $G(p, T)$ increase with pressure- p and decrease with temperature- T . Y also increases with the strain- η (strain-hardening). For Al6061 we take following Steinberg [19]:

$$Y_{mx} = 0.68, \beta = 125, n = 0.10, \frac{Y'_p}{Y_0} = \frac{G'_p}{G_0} = 0.065 \quad (63)$$

The critical wave length below which elastic flow will damp perturbations will be (see Eq. (47)):

$$\lambda_c = \frac{4\pi G}{\rho g} = \frac{124.5088}{g} \quad (64)$$

3.1. Overview of the $g = -0.1 \text{ mm}/\mu\text{s}^2$ simulations

The hydrostatic pressure at the AL-gas interface by Eq. (54) is $p_l = 0.15 \text{ GPa}$. For the hydrostatic pressure difference over h_0 we get from Eq. (55) $\Delta p_h = 0.00357$. Elastic flow will damp perturbations with wave length shorter than λ_c . From Eq. (47) we get $\lambda_c = 1245.1 \text{ mm}$. From Eq. (50), $\lambda_0 = 1/3 \text{ mm}$, thus we expect the RTI to grow only if (see Eq. (55)) $Y < 0.00357$.

In Fig. 7 we can see (up-down) the simulations with the yield strength of respectively $Y = 0, 10^{-5}, 10^{-2}, 0.3 \text{ GPa}$ at $T_{mx} = 10 \mu\text{s}$. Indeed, only for $Y \geq 10^{-2}$ we get significant instability growth. These are pure Lagrangian SMG calculations. For small deformations the scheme is much less dissipative than classical Lagrange calculations. Without strength or for low yield strength ($Y = 10^{-5}$) the SMG Lagrangian scheme is able to deal with the large deformations caused by the instability growth.

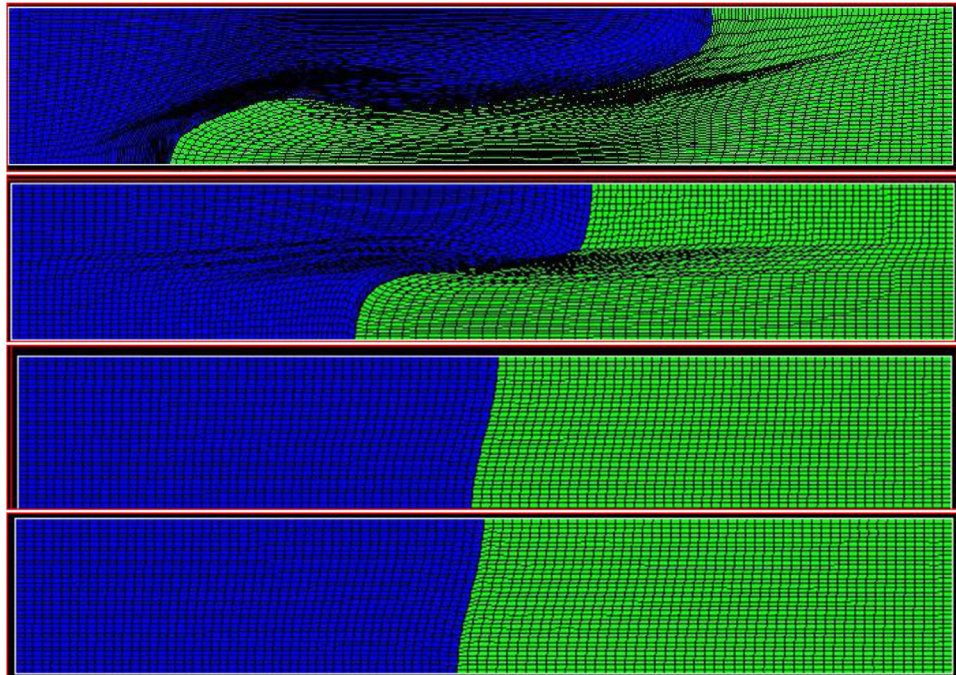


Fig. 7. Lagrangian $Y = 0, 10^{-5}, 10^{-2}, 0.3 \text{ GPa}$ calculations: $T = 10 \mu\text{s}$, $g = -0.1 \text{ mm}/\mu\text{s}^2$.

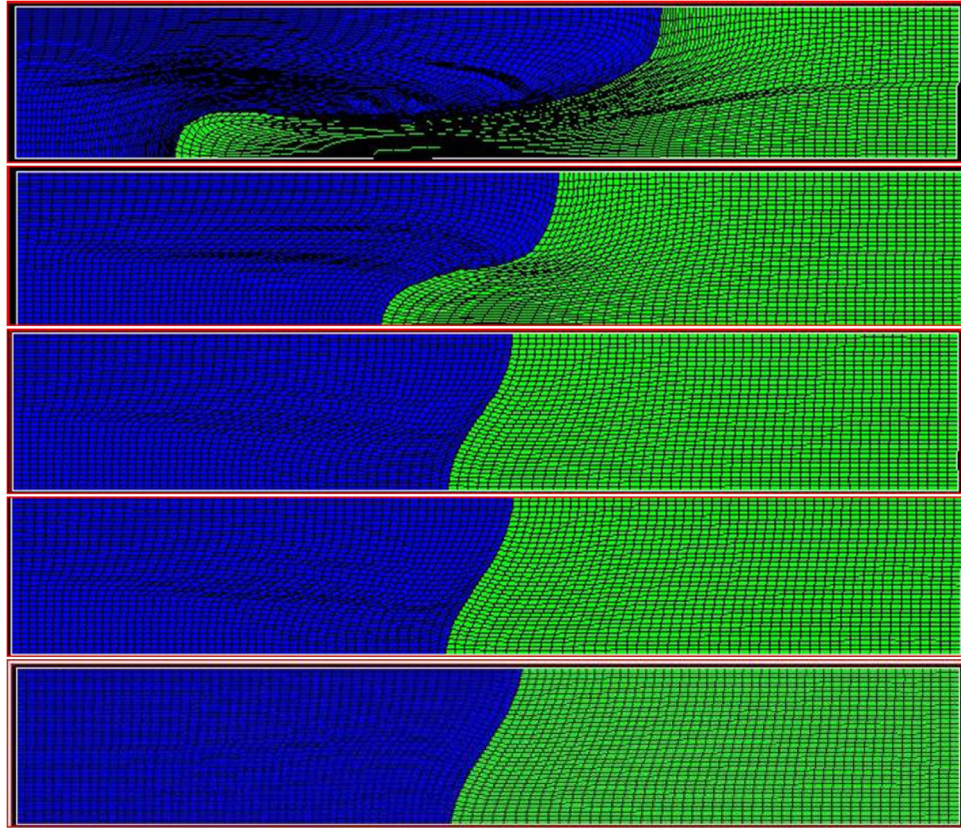


Fig. 8. Lagrangian $Y = 0, 0.1, 0.3, 0.5 \text{ GPa}$, $Y(p, \eta)$ calculations: $T = 1 \mu\text{s}$; $g = -10 \text{ mm}/\mu\text{s}^2$.

3.2. Overview of the $g = -10 \text{ mm}/\mu\text{s}^2$ simulations

In this case we get:

$$p_I \approx 15 \text{ GPa}, \Delta p_h = 0.357 \text{ GPa}, \lambda_c = 1.2451 \text{ mm} \quad (65)$$

As $\lambda_0 = 1/3$, again $\lambda_0 < \lambda_c$ and RTI growth is expected to be damped out in the elastic region. Only for $Y < 0.357 \text{ GPa}$ should the RTI growth prevail. To get to similar instability growth (see Eq. (62)) we run these calculations until $T_{mx} = 1 \mu\text{s}$. In Fig. 8 we show the mesh at $T_{mx} = 1 \mu\text{s}$ for the SMG Lagrangian calculations. These were carried out as shown up-down for yield strength of respectively $Y = 0, 0.1, 0.3, 0.5, Y(p, \eta)$. The last one in the lower frame is for $Y(p, \eta)$ using Steinberg et al. model Eqs. (60) and (61) with the parameters shown in Eq. (63). Indeed, we see significant instability growth only in the $Y = 0, 0.1 \text{ GPa}$ calculations. The SMG scheme can complete even the $Y = 0$ calculation, despite the observed large deformations.

3.3. Overview of the $g = -100 \text{ mm}/\mu\text{s}^2$ simulations

For $g = -100 \text{ mm}/(\mu\text{s})^2$ we get:

$$p_I \approx 150 \text{ GPa}, \Delta p_h = 3.57 \text{ GPa}, \lambda_c = 0.12451 \text{ mm} \quad (66)$$

$\lambda_0 = 1/3$, thus $\lambda_0 > \lambda_c$ and some RTI growth could be expected to occur also in the elastic region. As we expect larger deformations, we carry out the calculations with a MMALE mesh. Using Eq. (62) we should run these calculations until $T_{mx} = 1/\sqrt{10} = 0.31 \mu\text{s}$. In Fig. 9 we show the mesh and material interfaces at $T_{mx} = 0.28 \mu\text{s}$ for the SMG MMALE calculations. From top to bottom, they are for $Y = 0, Y = 1, Y = 1.4, Y = 1.6 \text{ GPa}$. Let us note that here the instability growth in the simulation is damped out already at $Y = 1.6 \text{ GPa}$, at somewhat lower Y than expected ($Y = 3.57 \text{ GPa}$) from the simple model of Eq. (46).

3.4. Comparing Lagrangian and MMALE $g = -100 \text{ mm}/\mu\text{s}^2$ SMG simulations

The Lagrangian SMG scheme is robust and can carry out calculations which would fail in a classical Lagrangian scheme. This is mainly due to its hourglass damping capability (see Fig. 3). Moreover these terms arise naturally from the conservation laws and do not have artificial parameters. However, their effect of mesh stabilizing could generate some mesh imprinting for very distorted meshes. On one hand the MMALE scheme with its interface reconstruction can deal with arbitrary large deformations but on the other hand it can be much more dissipative. By comparing the two we can measure how dissipative is the MMALE scheme for lower deformations and how stiff becomes the Lagrangian scheme in a distorted mesh with long and thin zones. In Fig. 10 we compare Lagrangian and MMALE calculations for $g = -100 \text{ mm}/\mu\text{s}^2$, $Y = 1.0 \text{ GPa}$ at $T = 0.28$. We can see that the large scale penetration is similar, but that the Lagrangian calculation, while robust, prevents the formation of small scale vortices at the penetrating head. Before this stage arrives it is beneficial to pass to a MMALE calculation. In Fig. 11 we compare Lagrangian and MMALE calculations for $g = -100 \text{ mm}/\mu\text{s}^2$, $Y = 1.4 \text{ GPa}$ at $T = 0.28$. As the yield strength is higher, the instability growth is slower and both calculations give similar results. In this cases we prefer the Lagrangian calculations. They are computationally more efficient, less dissipative and can better follow the interface motion.²

² While the MMALE interfaces cut through the mesh and are composed of distinct segments, the Lagrangian interface are defined on mesh lines (or mesh surfaces in 3D) and move with the mesh points without need of additional interpolations.

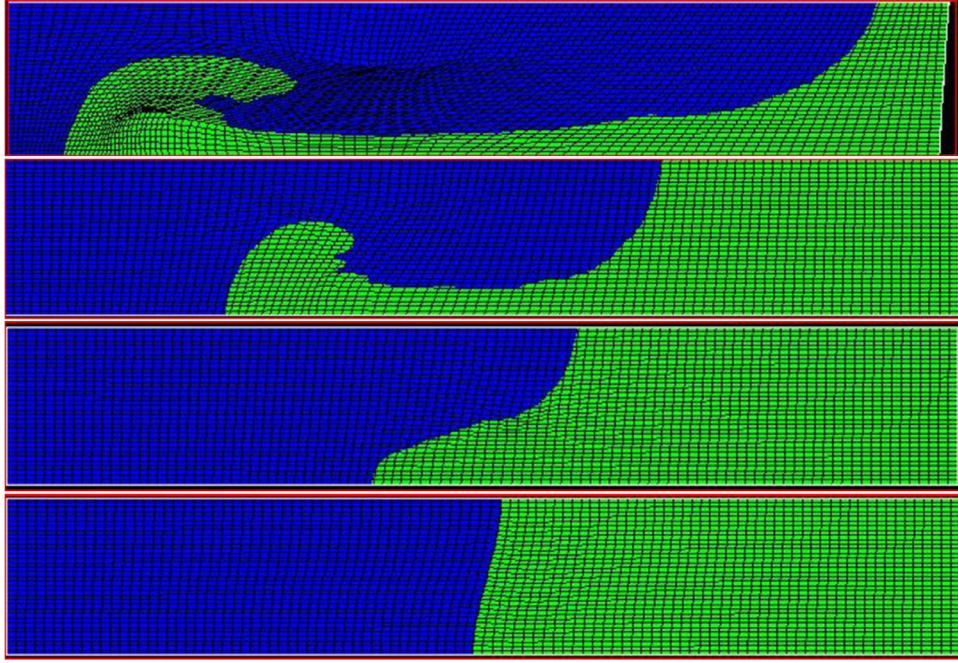


Fig. 9. MMALE $Y = 0, 1.0, 1.4, 1.6$ GPa calculations: $T = 0.28 \mu\text{s}$, $g = -100 \text{ mm}/\mu\text{s}^2$.

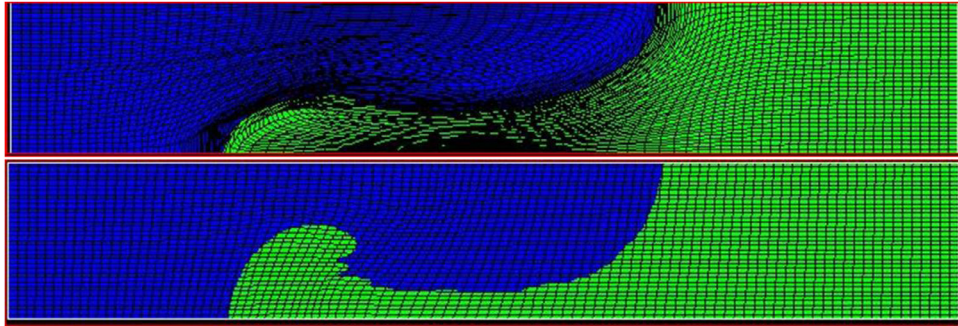


Fig. 10. Lagrangian (Upper) and MMALE (Lower) calculations: $T = 0.28 \mu\text{s}$, $g = -100 \text{ mm}/\mu\text{s}^2$, $Y = 1.0$ GPa.

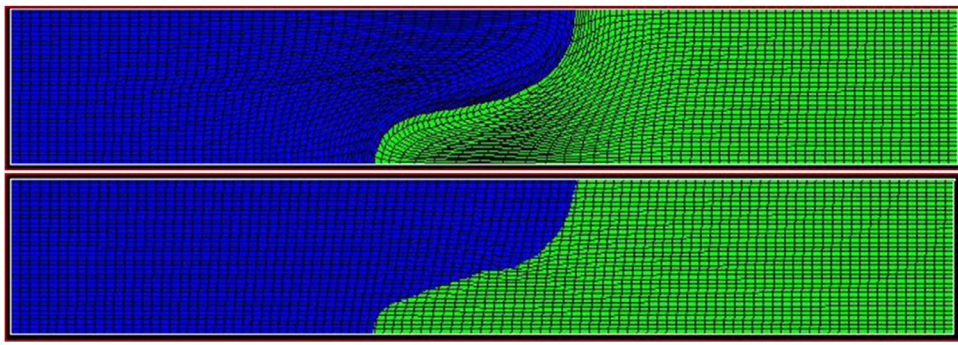


Fig. 11. Lagrangian (upper) and MMALE (lower) calculations at $T = 0.28 \mu\text{s}$, $g = -100 \text{ mm}/\mu\text{s}^2$, $Y = 1.4$ GPa.

3.5. Replacing ideal gas with water for the $\rho = 1 \frac{\text{mg}}{\text{mm}^3}$ layer in $g = -10 \text{ mm}/\mu\text{s}^2$, $Y = 0.3$ GPa Lagrangian simulations

For water we took a Mie-Gruneisen shock EOS with the parameters: $c_0 = 1.48 \frac{\text{mm}}{\mu\text{s}}$, $\Gamma = 0.5$, $s = 1.74$. In Fig. 12 we can see the results. While the gas is more compressible, the perturbation growth is dominated by the yield strength of the Al layer. A double layer made of water and Aluminum could also serve as a test case to study the effect of strength. The material parameters taken

here for water did not take into account effects like the change in the Gruneisen Γ of water with pressure and temperature.

4. Discussion and conclusions

The SMG scheme was applied to study RTI growth in solids. It can handle problems which would otherwise fail in classical Lagrange codes. It uses frame-invariant, VIP limiters for vectors and oriented bounding box based limiters for tensors. In it's MMALE

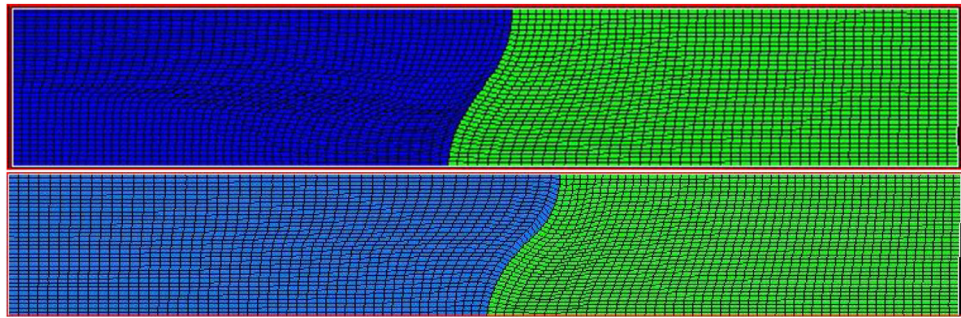


Fig. 12. Lagrangian $Y = 0.3$ GPa gas (upper) and water(lower) EOS calculations: $T = 1$ μ s, $g = -10$ mm/ μ s 2 .

phase, it can handle even larger deformations. A simple test case has been set-up to study RTI growth in solids. It extends to solids a well known test case for RTI growth in fluids. Earth gravity is replaced by a larger acceleration for which RTI growth is observed in solids. The resulting test case provides a simple, quick and reproducible way to study RTI growth dependence on material (e.g. $Y, G, \eta, \dot{\eta}$) and numerical parameters (e.g on the mesh and on the scheme).

In memoriam

This paper is dedicated to the memory of Dr. Douglas Nelson Woods (*January 11th 1985–†September 11th 2019), promising young scientist and post-doctoral research fellow at Los Alamos National Laboratory. Our thoughts and wishes go to his wife Jessica, to his parents Susan and Tom, to his sister Rebecca and to his brother Chris, whom he left behind.

Declaration of Competing Interest

The authors declare that they have no known competing financial interests or personal relationships that could have appeared to influence the work reported in this paper.

CRediT authorship contribution statement

Gabi Luttwak: Conceptualization, Methodology, Software, Data curation, Writing - review & editing.

References

- [1] Rayleigh L, Strutt JW. Investigation of the character of the equilibrium of an incompressible heavy fluid of variable density. In: Proceedings of the London mathematical society, 14; 1883. p. 170–7.
- [2] Taylor sir GI. The instability of liquid surfaces when accelerated in a direction perpendicular to their planes. In: Proc. roy. soc. (London), vol. A 201; 1950. p. 192–6.
- [3] Luttwak G, Falcovitz J. Staggered mesh godunov (SMG) schemes for Lagrangian hydrodynamics. In: Furnish MD, editor. Shock compression of condensed matter-2005; 2006. p. 339–42. AIP, CP845
- [4] Luttwak G, Falcovitz J. Staggered mesh godunov (SMG) schemes for ALE hydrodynamics. Workshop on numerical methods for multi-material flows. Oxford, UK, Sept.; 2005. <http://www.extra.rdg.ac.uk/ifcd/Multimaterial-Workshop.htm>
- [5] Loubere R, Maire PH, Shashkov M, Breil J, Galera S. ReALE a reconnection based ALE method. *J Comput Phys* 2010;229:4724–61.
- [6] Luttwak G, Falcovitz J. Slope limiting for vectors: a novel vector limiting algorithm. *Int J Numer Meth Fluids* 2011;65:1365–75.
- [7] Luttwak G, Falcovitz J. VIP (vector image polygon) limiters in ALE hydrodynamics. *Eur Phys J - EPJ Web of Conferences* 2010;10:00020.
- [8] Luttwak G. On the extension of monotonicity to multidimensional flows. Int conf on num methods for multi-material fluid flow (MULTIMAT 2015), Wurzburg, Germany; 2015. http://dy123d.com/gabilut_files/papers/monotonicity_in_multidim.pdf.
- [9] Dimonte G. Nonlinear evolution of the Rayleigh-Taylor and Richtmyer-Meshkov instabilities, presented at 40th annual meeting of the american physical society. Division of plasma physics new orleans, LA,(1998) LLNL report UCRL-JC-132439; 1998.
- [10] Polavarapu R, Roach P, Banerjee A. Rayleigh-Taylor-instability experiments with elastic-plastic materials. *Phys Rev E* 2019;99:053104.
- [11] Barnes JF, Blewett PJ, McQueen RG, Meyer KA, Venable D. Taylor instability in solids. *J Appl Phys* 1974;45(2):727–32.
- [12] Dimonte G, Gore R, Schneider M. Rayleigh-Taylor instability in elastic-plastic materials. *Phys Rev Lett* 1998;80(6):1212–15.
- [13] Robinson AC, Swegle JW. Acceleration instability in elastic-plastic solids. II. Analytical techniques. *J Appl Phys* 1989;66(7):2859–72.
- [14] Swegle JW, Robinson AC. Acceleration instability in elastic-plastic solids. I. Numerical simulations of plate acceleration. *J Appl Phys* 1989;66(7):2838.
- [15] Park HS, et al. Strong stabilization of the Rayleigh-Taylor instability by material strength at megabar pressures. *Phys Plasmas* 2010;17:056314.
- [16] Barton NR, et al. A multiscale strength model for extreme loading conditions. *J Appl Phys* 2011;109:073501.
- [17] Mikaelian KO. Design of a Rayleigh-Taylor experiment to measure strength at high pressures. *Phys Plasmas* 2010;17:092701.
- [18] Johnson GR, Cook WH. A constitutive model and data for metals subjected to large strains, high strain rates and high temperatures. In: Proc. 7th international symposium on ballistics 1983; 1983. p. 54–547.
- [19] Steinberg DJ, et al. A constitutive model for metals applicable at high strain rate. *J Appl Phys* 1980;51:1498.
- [20] Luttwak G, Rosenberg Z, Falcovitz J. Experimental and computational study of taylor impact with square rods. In: Proceedings 15th int. symposium on ballistics, Jerusalem, I; 1995. p. 291–8.
- [21] Steinberg DJ, Lund CM. A constitutive model for strain rates from 10^{-4} to 10^6 s $^{-1}$. *J Appl Phys* 1989;65:1528.
- [22] Preston DL, Tonks DL, Wallace DC. Model of plastic deformation for extreme loading conditions. *J Appl Phys* 2003;93:211.
- [23] Zerilli FJ, Armstrong RW. Dislocation-mechanics-based constitutive relations for material dynamics calculations. *J Appl Phys* 1987;61(5):1816–25.
- [24] Follansbee PS, Kocks UF. A constitutive description of the deformation of copper based on the use of the mechanical threshold stress as an internal state variable. *Acta Metall* 1988;36(36):81–93.
- [25] Kanel GI. Rate and temperature effects on the flow stress and tensile strength of metals. In: AIP conference proceedings, 1426; 2012. p. 939–44.
- [26] Miles JW. Taylor instability of a flat plate. General dynamics rep. GAMD-7335, AD643161; 1966.
- [27] Drucker DC. Taylor instability of a surface of an elastic-plastic plate. In: Nemat-Nasser, editor. Mechanics today, 5. Pergamon Press; 1980. p. 37–47.
- [28] Cela JJL, Piriz AR, Temporal M, Tahir NA, Moreno MCS. Elasto-plastic effects on the Rayleigh-Taylor instability in an accelerated solid slab. *Eur Phys J Appl Phys* 2005;29:247–52.
- [29] Piriz AR, Cela JJL, Tahir NA. Rayleigh-Taylor instability in elastic-plastic solids. *J Appl Phys* 2009;105:116101.
- [30] Colvin JD. A model for instability growth in accelerated solid metals. *J Appl Phys* 2003;93:5287.
- [31] Sun Y. Rayleigh Taylor instability in accelerated high energy density matter. University of Castilla-La Mancha, Ciudad Real, Spain; 2016. Ph.D. thesis.
- [32] Bai X, Wang T, Zhu Y, Luo G. Rayleigh - expansion of linear analysis of Rayleigh-Taylor interface instability of metal materials. *World J Mech* 2018;8:94–106.
- [33] Youngs DL. Numerical simulation of turbulent mixing by Rayleigh-Taylor instability. *Phys D* 2004;12:32–44.
- [34] Dimonte G, et al. A comparative study of the turbulent Rayleigh-Taylor instability using high-resolution three-dimensional numerical simulations: the alpha-group collaboration. *Phys Fluids* 2004;16(5):1668–93.
- [35] Glimm J, Sharp D, Kaman T, Lim H. New directions for Rayleigh-Taylor mixing. *Philos Trans R Soc* 2013;A 371:20120183.
- [36] Luttwak G, Falcovitz J. Rayleigh taylor instability growth using the staggered mesh godunov scheme. ISCM-36, Israel assoc. comp. meth. in mechanics, IACMM, Haifa, Israel; 2014. http://www.dy123d.com/gabilut_files/ppt-pdf/isham-haifa-2014-cor-01.pdf
- [37] Caramana EJ, Shashkov MJ, Whalen RP. Formulations of artificial viscosity for multi-dimensional shock wave computations. *J Comput Phys* 1998;144:70–97.
- [38] Christensen RB. Godunov methods on a staggered mesh. an improved artificial viscosity. LLNL report UCRL-JC-105269; 1990.

- [39] de Frahan MTH, et al. Experimental and numerical investigations of beryllium strength models using the Rayleigh-Taylor instability. *J Appl Phys* 2015;117:225901.
- [40] Wilkins ML. Methods in computational physics. In: Calculation of elastic-plastic flow, 3. Academic Press; 1964. p. 211–63.
- [41] Maire PH, Abgrall R, Breil J, Loubere R, Reboulet B. A nominally second-order cell-centered Lagrangian scheme for simulating elastic-plastic flows on two-dimensional unstructured grids. *J Comput Phys* 2013;235:626–65.
- [42] Luttwak G, Falcovitz J. VIP (vector image polygon) multi-dimensional slope limiters for scalar variables. *Comput Fluids* 2013;83:90–7.
- [43] Luttwak G, Falcovitz J. Applying the staggered mesh gogunov (SMG) method to reactive flows. *Int J Energy Mat* 2010;28(s1):271–302. Presented at 7th Int. Conf. on New Models and Hydro-codes, Lisbon, Portugal, 2008
- [44] Luttwak G. Partially split volume integration scheme for the advection phase of Eulerian and MMALE simulations. Int conf new models and hydrocodes for shock wave processes, Univ of Maryland, College Park,MD; 2004. http://www.dy123d.com/gabilut_files/ppt-pdf/splitadv-shock04.pdf
- [45] Luttwak G, Hillel S, Falcovitz J. A lump-consistent remap scheme for ALE hydrodynamics. Presented at advances in computational mechanics, omni hotel, San-Diego,CA, USA; 2013. http://dy123d.com/gabilut_files/papers/lump_consistent_remapping.pdf
- [46] Luttwak G. Numerical simulation of water jet penetration. In: Asay JR, editor. Shock waves in condensed matter-1983. Elsevier Science Publishers; 1984. p. 191–4.
- [47] Luttwak G, Rabie RL. The multi-material arbitrary Lagrangian Eulerian code MMALE and its application to some problems of penetration and impact. LANL report LA-UR-85-2311; 1985.
- [48] Luttwak G. Interface tracking in Eulerian and MMALE calculations. In: Furnish MD, editor. Shock compression of condensed matter-2001, AIP, CP620; 2002. p. 283–6.
- [49] Maire PH. High-order cell-centered Lagrangian scheme for two-dimensional compressible fluid flows on unstructured meshes. *J Comput Phys* 2009;228(7):2391–425.
- [50] Luttwak G. On rules for grid motion in three dimensional arbitrary Lagrangian Eulerian codes. *Khimicheskaya Fizika (Russian Journal of Physical Chemistry B)* 2006;25(5):54–9. Presented at the New Models and Hydro-codes for Shock Wave Processes 2002, Edinburgh, Scotland, UK http://dy123d.com/gabilut_files/papers/On_rules_for_ALE.pdf
- [51] Winslow AM. Equipotential zoning of two dimensional meshes. *J Comput Phys* 1966;1:149.
- [52] Knupp P, Margolin L, Shashkov M. Reference Jacobian optimization-based re-zone strategies for arbitrary Lagrangian Eulerian methods. *J Comput Phys* 2002;176(1):93–128.